Supporting Information for

Tuning Product Selectivity in Direct Electroreduction of NO via Phase Engineering of MoS_2 Nanosheets in Water-fed PEM Electrolyzer

Min Li, [a,c] Frank Hernandez Baena, [a] Shota Matsuo, [a] Mingliang Chen, [a] Boaz Izelaar, [b,c] Ruud Kortlever, [b,c] and Atsushi Urakawa *[a, c]

[a]Department of Chemical Engineering, Delft University of Technology, Van der Maasweg 9, 2629 HZ, Delft, the Netherlands
[b]Department of Process & Energy, Delft University of Technology, Leeghwaterstraat 39, 2628 CB, Delft, the Netherlands
[c]e-Refinery Institute, Delft University of Technology, Leeghwaterstraat 39, 2628 CB Delft, the Netherlands

Corresponding Author: A.Urakawa@tudelft.nl

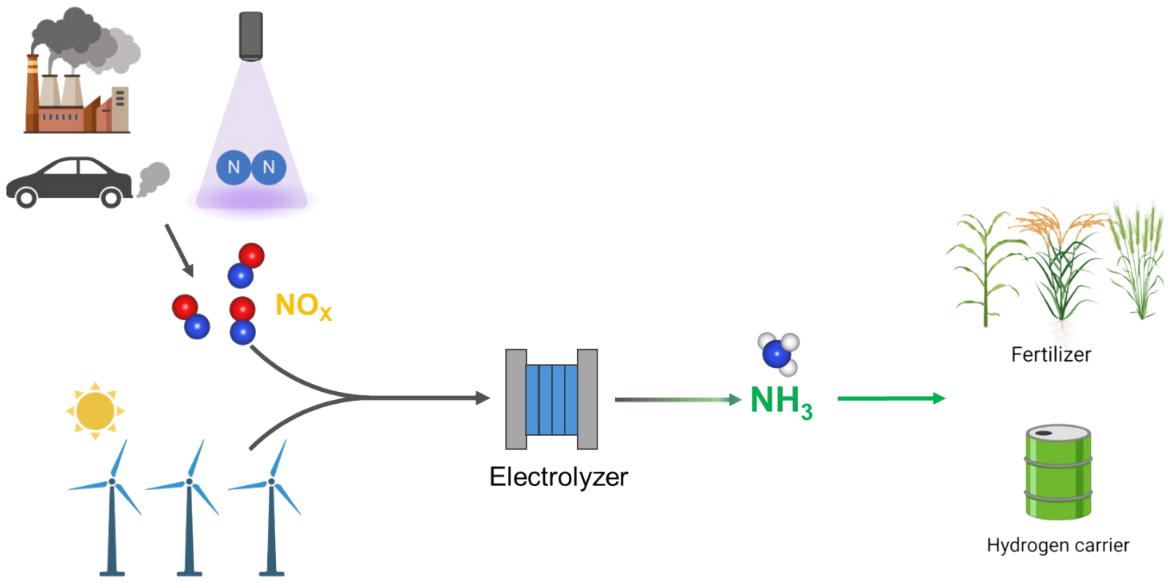

Figure S1. Schematic of electrochemical NO_x reduction for ammonia production.

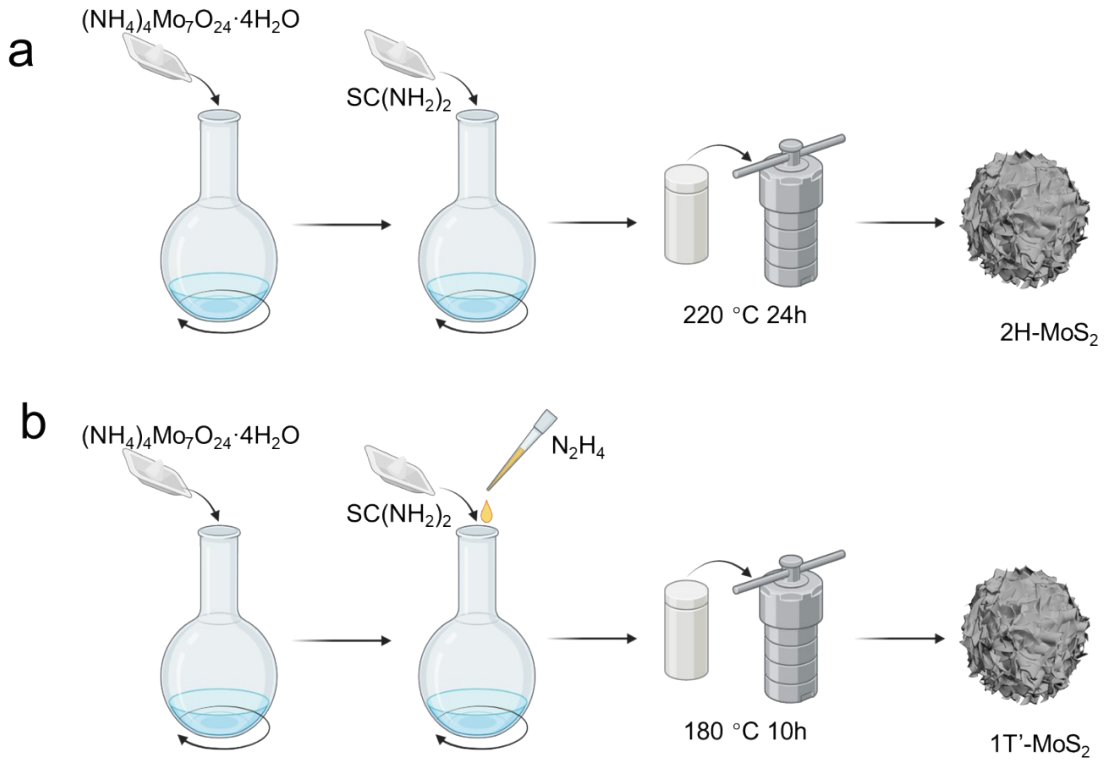

Figure S2. MoS_2 hydrothermal synthesis protocol (a) 2H-MoS_2 and (b) 1T'-MoS_2.

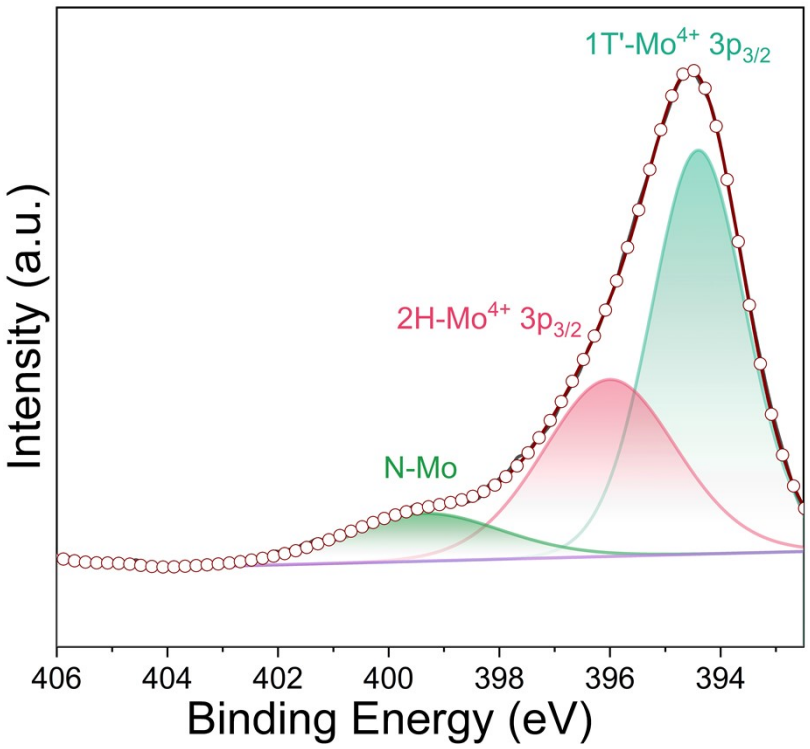

Figure S3. XPS spectra associated with N (1s) for 1T'-MoS_2.

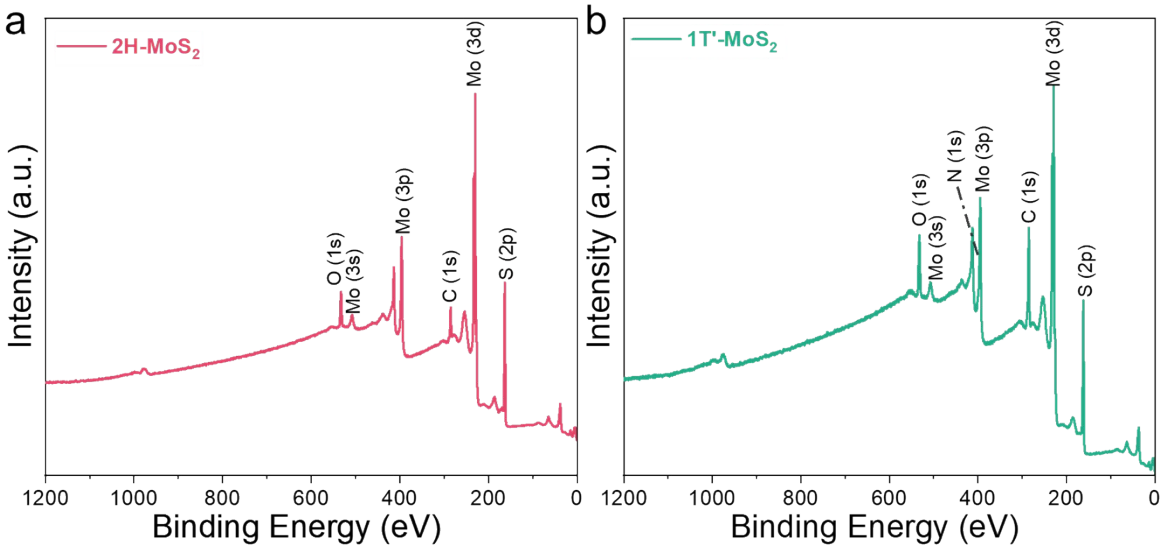

Figure S4. XPS survey scan of (a) 2H-MoS_2 and (b) 1T'-MoS_2.

Table S1. Elemental analyses of 2H and 1T' phases of MoS_2 using XPS

Catalyst	Atomic percentage of Mo	Atomic percentage of S	Atomic ratio
2H-MoS_2	35%	65%	1:1.86
1T'-MoS_2	38%	62%	1:1.63

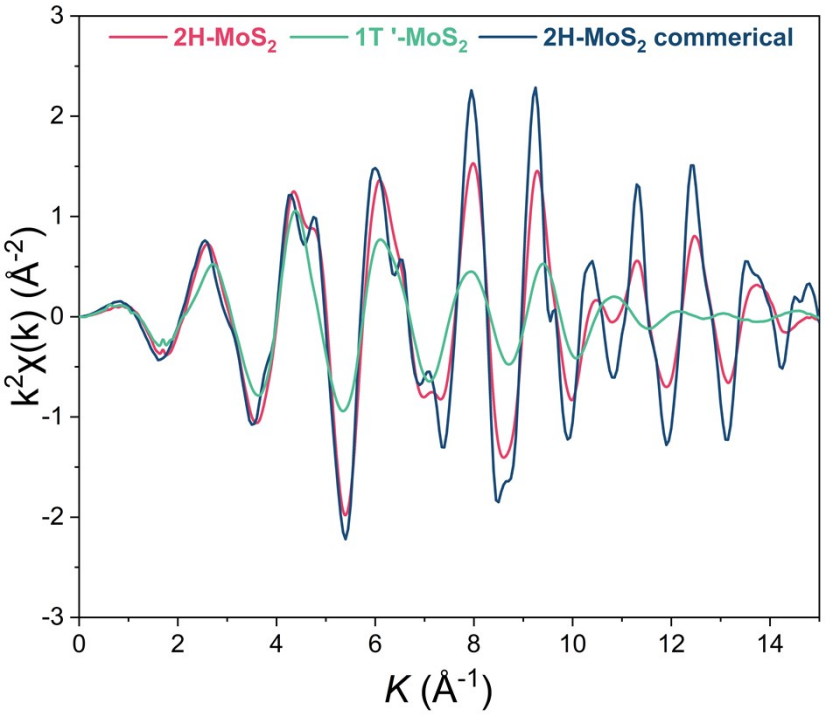

Figure S5. Mo K-edge oscillation functions $k^2\chi(k)$ for MoS_2 samples.

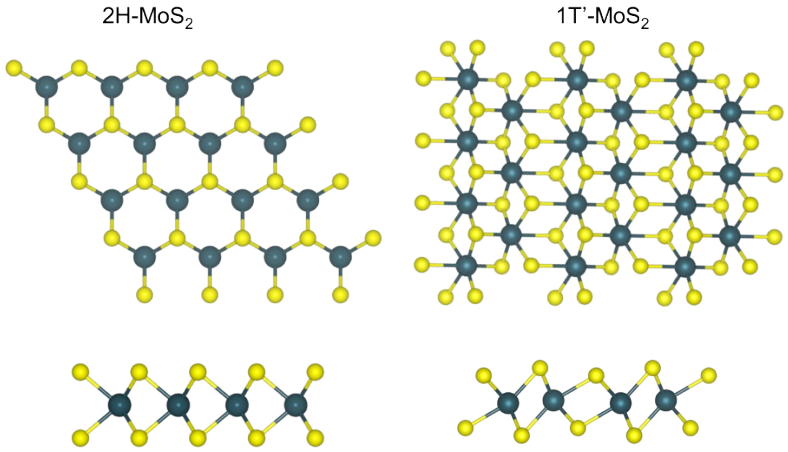

FigureS6. The atomic models of 2H and 1T' phases of MoS_2. Upside: top view of the structure; downside: side view of the structures.

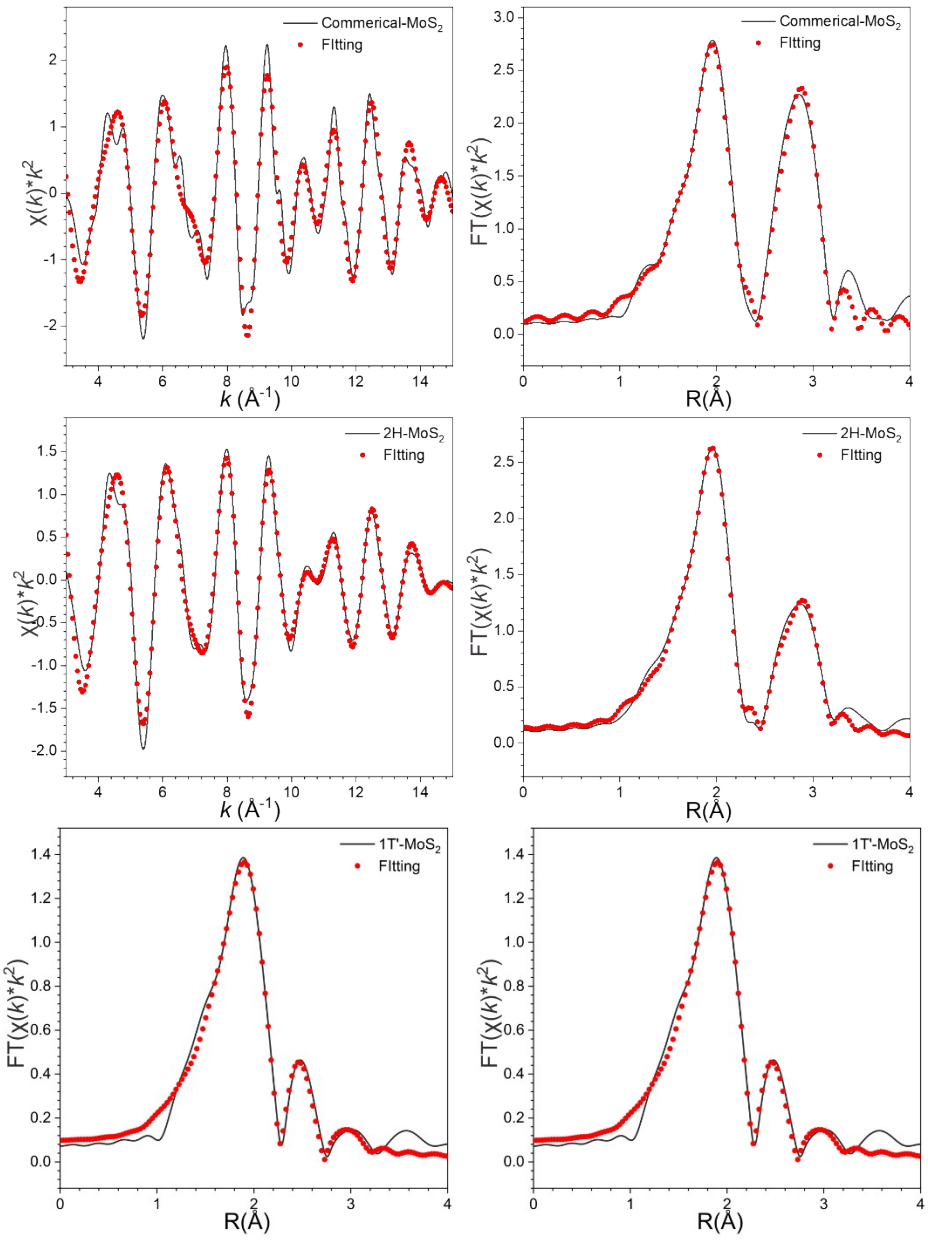

Figure S7. (a) Fitting curves for EXAFS data at the Mo K-edge for (a & b) commercial MoS_2; (c & d) 2H-MoS_2 and (e & f) 1T'-MoS_2, respectively.

Table S2. Curve fit parameters for Mo K-edge EXAFS for MoS_2 samples

Sample	Path	E_0 (eV)	*N*	R / Å	σ^2 / Å^2	R factor
MoS_2 commercial	Mo-S	1±1	5.1(4)	2.41(1)	0.002(1)	0.0012
	Mo-Mo		6.0(1)	3.17(2)	0.003(1)	
2H-MoS_2	Mo-S	2±1	5.7(3)	2.41(1)	0.003(1)	0.0009
	Mo-Mo		4.5(8)	3.17(2)	0.004(1)	
1T'-MoS_2	Mo-S	0±1	4.6(4)	2.40(1)	0.007(1)	0.0016
	Mo-Mo		0.8(5)	2.77(3)	0.004(1)	

* S_0^2 was fixed as 0.9 and determined through fitting of a Mo foil using an available standard Mo.cif (mp-129). Data ranges: $3 \leq k \leq 15$ Å, $1.0 \leq R \leq 3.3$ Å. The total number of independent data points were 15.8, 17.3 and 17.3 for MoS_2 commercial, 2H-MoS_2 and1T'-MoS_2, respectively.

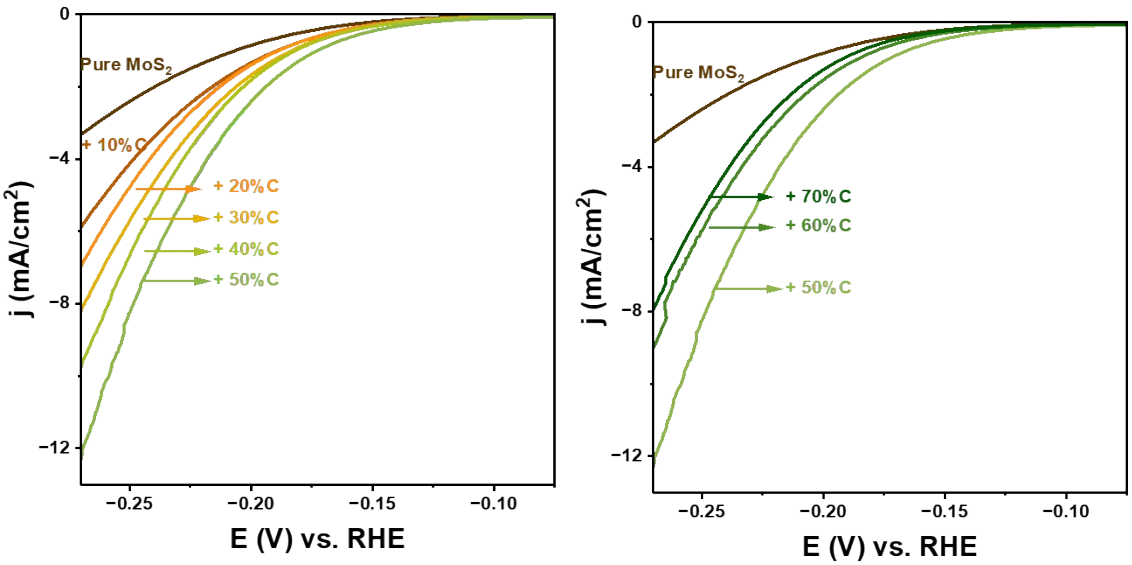

Figure S8. LSV curves of 2H-MoS_2 with different carbon ratio in 0.1 M H_2SO_4 electrolyte.

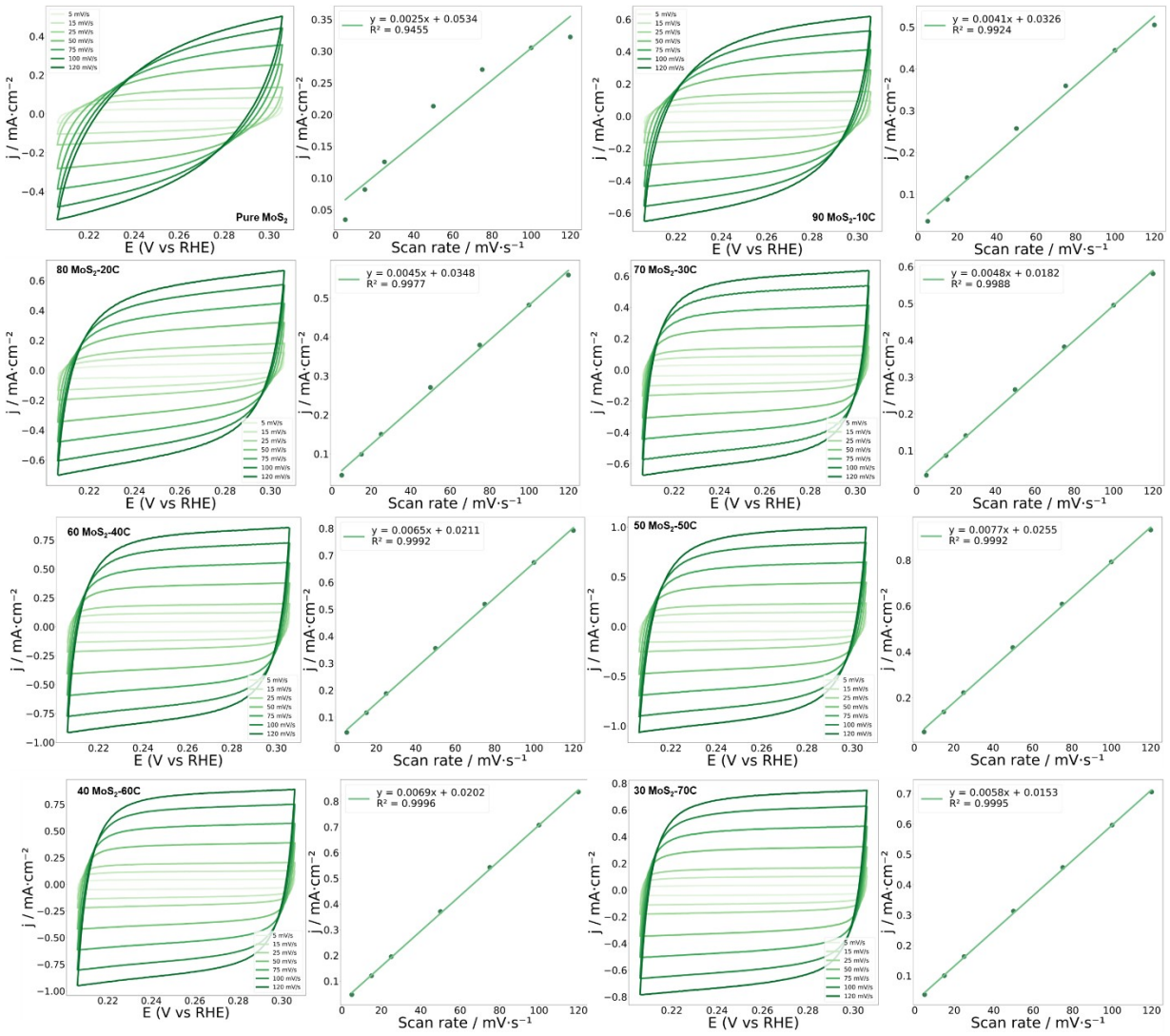

Figure S9. CV curves for Cdl at different scan rates (5–120 mV·s^{-1}); (b) electrochemical double layer capacitance (Cdl) for 2H-MoS_2 with different carbon ratios.

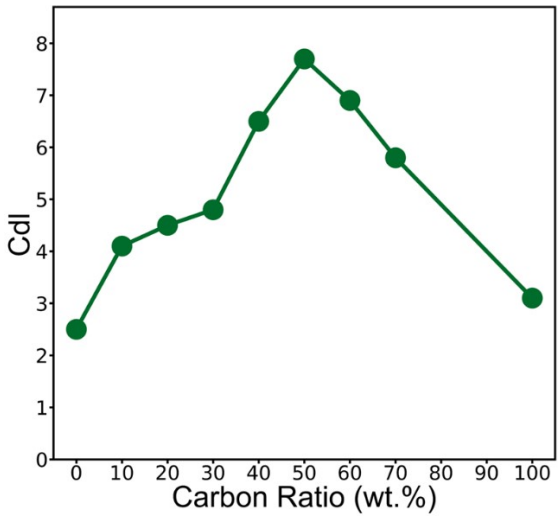

Figure S10. Comparasion of electrochemical double layer capacitance (Cdl) for 2H-MoS_2 with different carbon ratios.

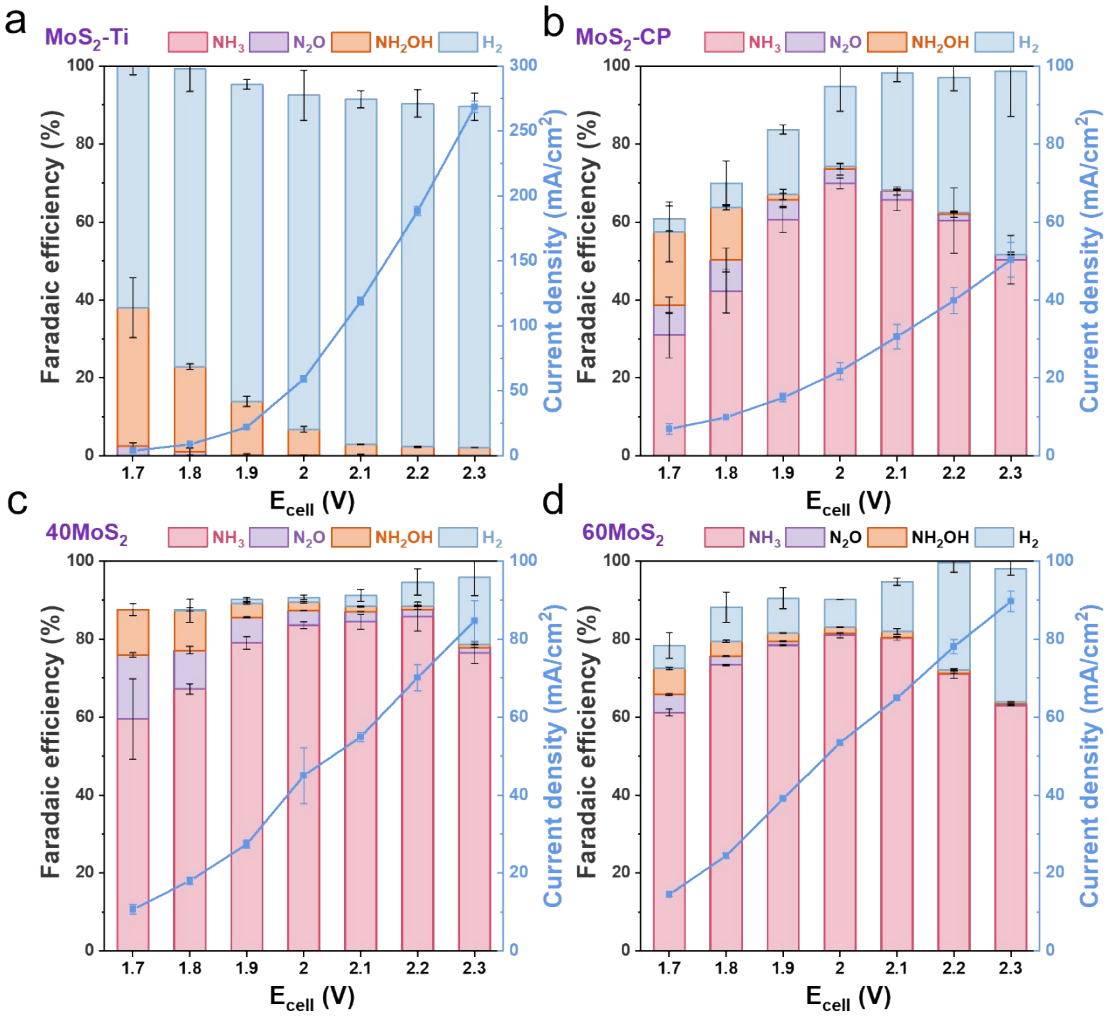

Figure S11. Faradaic efficiency for electrocatalytic NORR as a function of cell voltage (1.7 to 2.3 V) for (a) Pure MoS_2 with Ti GDL; (b) pure MoS_2; (c) $40MoS_2$/60C; (d) $60MoS_2$/40C with carbon paper.

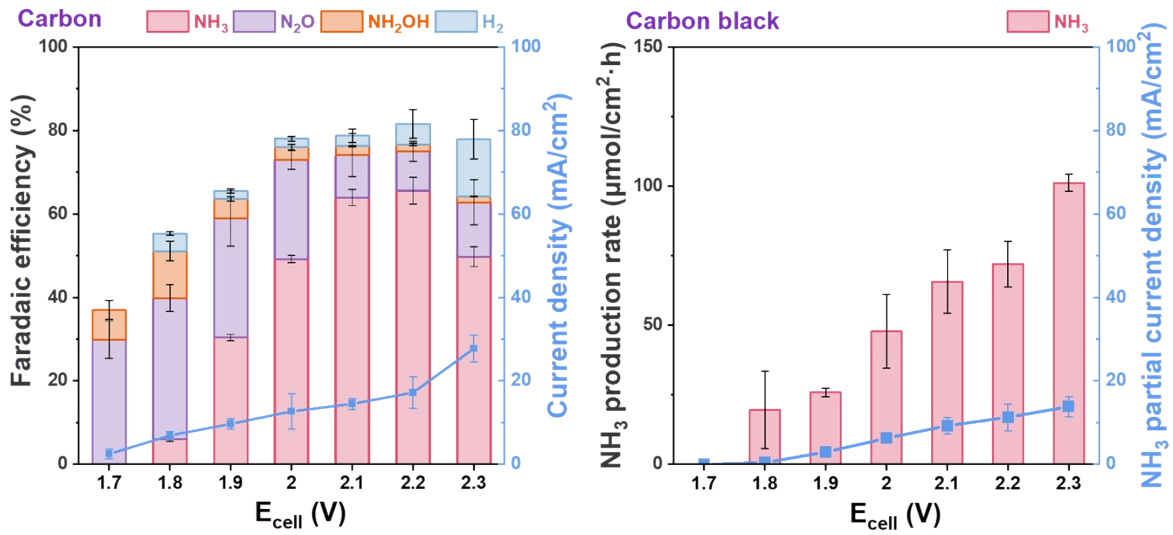

Figure S12. (a) Faradaic efficiency; (b) ammonia production rate for electrocatalytic NORR as a function of cell voltage (1.7 to 2.3 V) for carbon black.

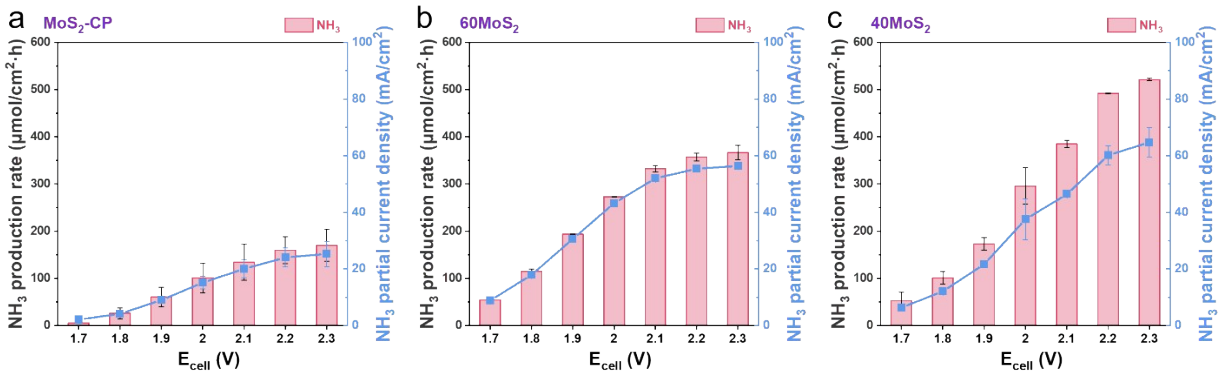

Figure S13. Ammonia production rate and partial current density for (a) MoS_2 with carbon paper (CP); (b) $60MoS_2/40C$ with carbon paper and (c) $40MoS_2/60C$ with carbon paper.

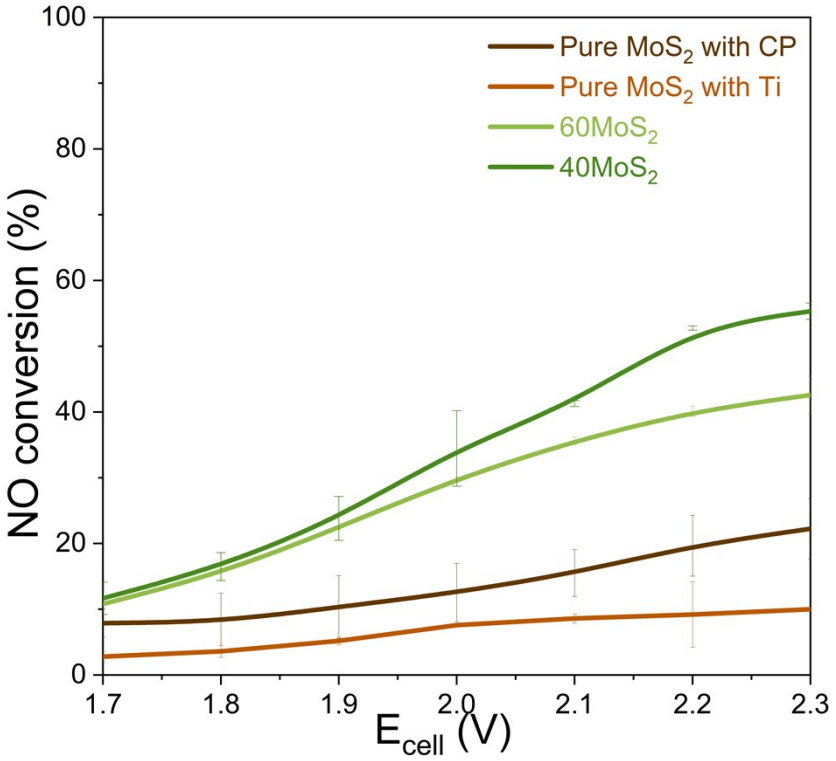

Figure S14. Single pass NO conversion rate.

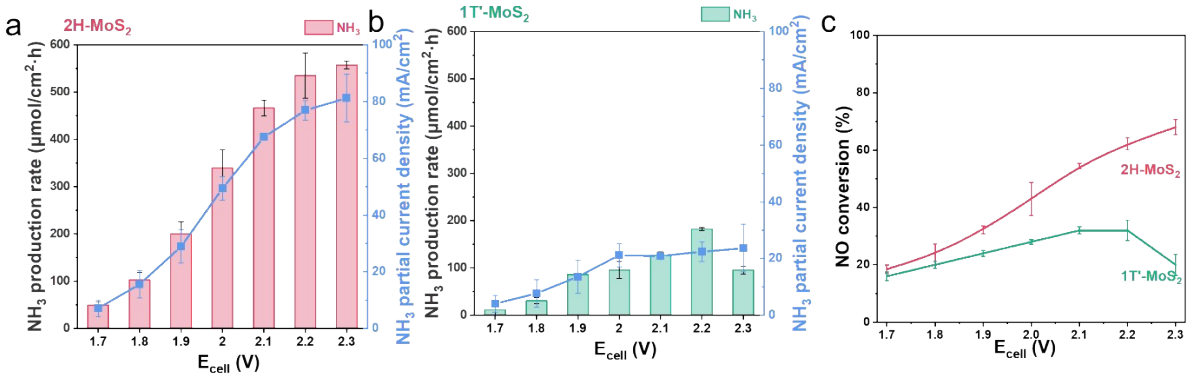

Figure S15. Ammonia production rate and partial current density on (a) 2H- and (b)1T'-MoS_2; (c) NO conversion.

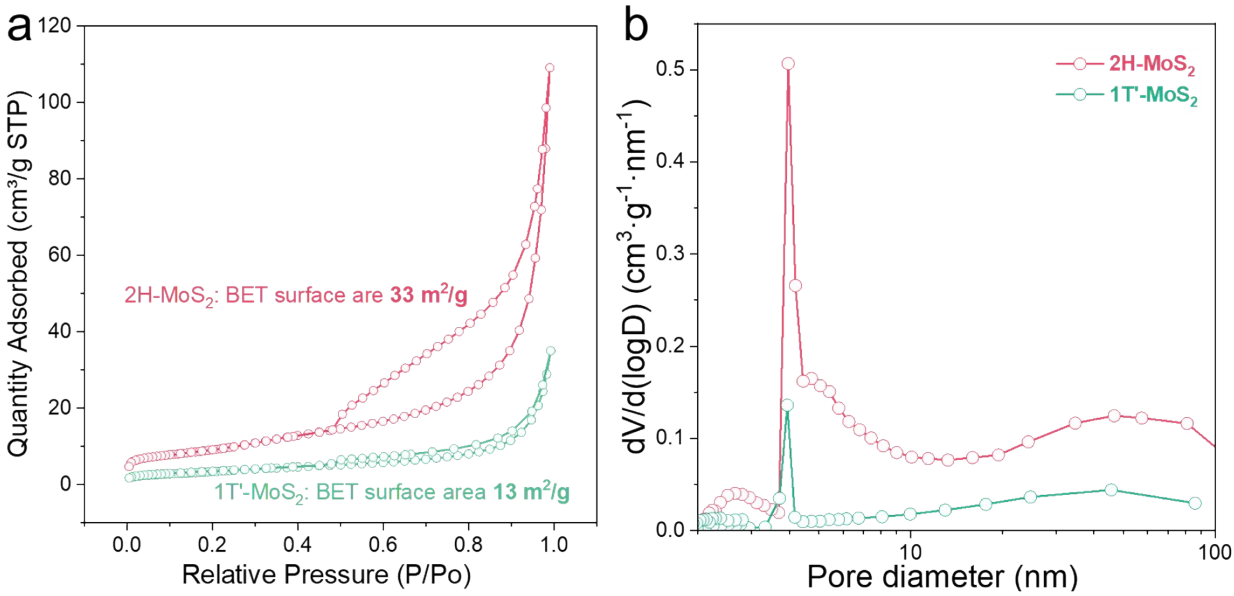

Figure S16. (a) BET surface area and (b) pore-size distribution curves of as-prepared 2H- and 1T'-MoS_2 samples.

Table S3. Relative atomic percentage distribution of Mo for 2H and 1T' - MoS_2 using XPS

Sample	Relative atomic percentage of Mo			
	1T	2H	Mo^{5+}	Mo^{6+}
2H-MoS_2-Fresh		94%		6%
2H-MoS_2-Used		66%	11%	23%
1T'-MoS_2-Fresh	80%	15%	3%	2%
1T'-MoS_2-Used	22%	22%	16%	40%

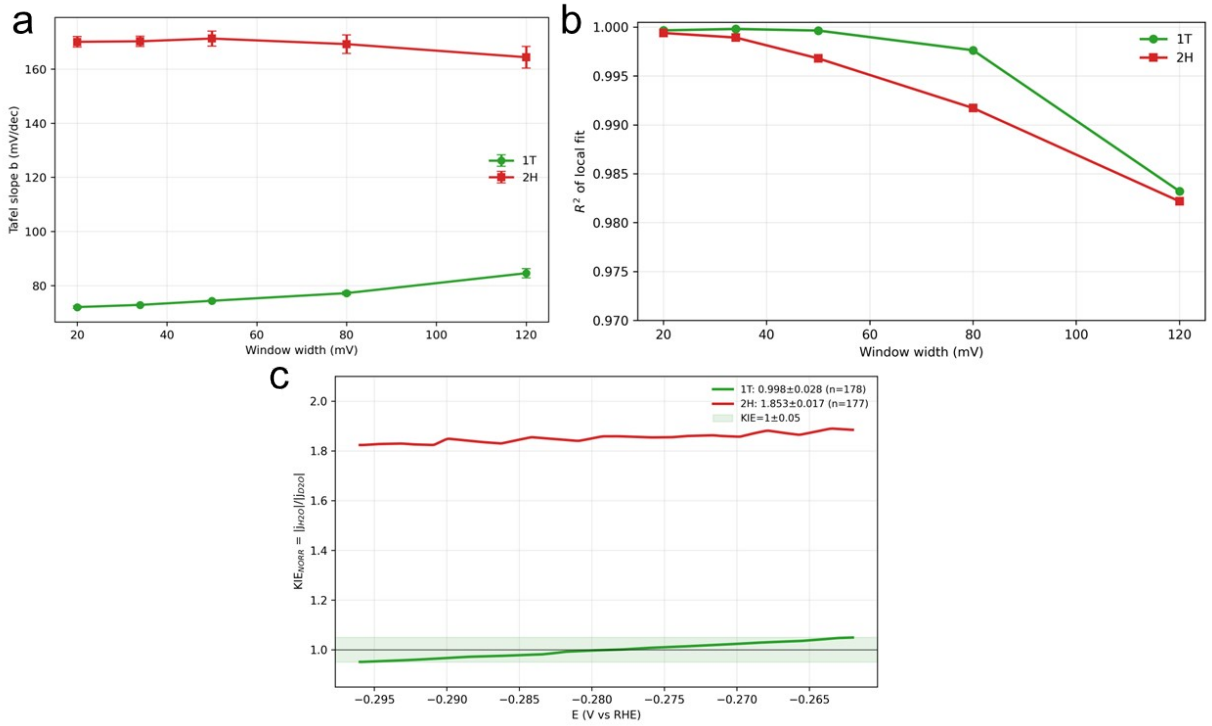

Figure S17. (a) Window-width sensitivity and (b) fitting linearity R^2 of extracted local Tafel slopes; (c) apparent KIE values across the window.

A potential window (E_RHE = −0.296 to −0.262 V) was selected to ensure a locally consistent kinetic regime. Within this window, the local Tafel representation (η* = -E_RHE vs log|j|) remains highly linear (high R^2), and the local derivative d(log|j|)/dE is comparatively stable, minimizing regime mixing in the extracted kinetic descriptors. The robustness of the extracted local Tafel slopes was further assessed by varying the window width around the same center potential: the fitted slopes remain essentially unchanged for moderate window widths (20-80 mV), whereas substantially wider windows (e.g., 120 mV) reduce linearity and indicate mixing of kinetic regimes. Extending the analysis to more negative potential is also avoided because it increases the likelihood of competing-current contributions (e.g., HER) and additional regime transitions that can confound interpretation.

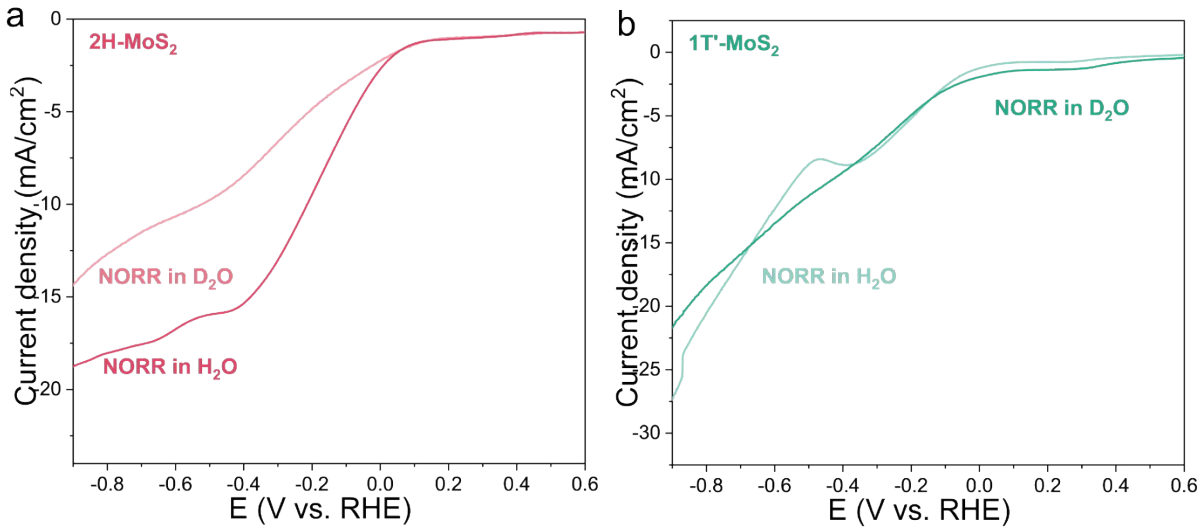

Figure S18. (a) and (b) LSV scan for 2H- and 1T'-MoS_2 in a batch cell.

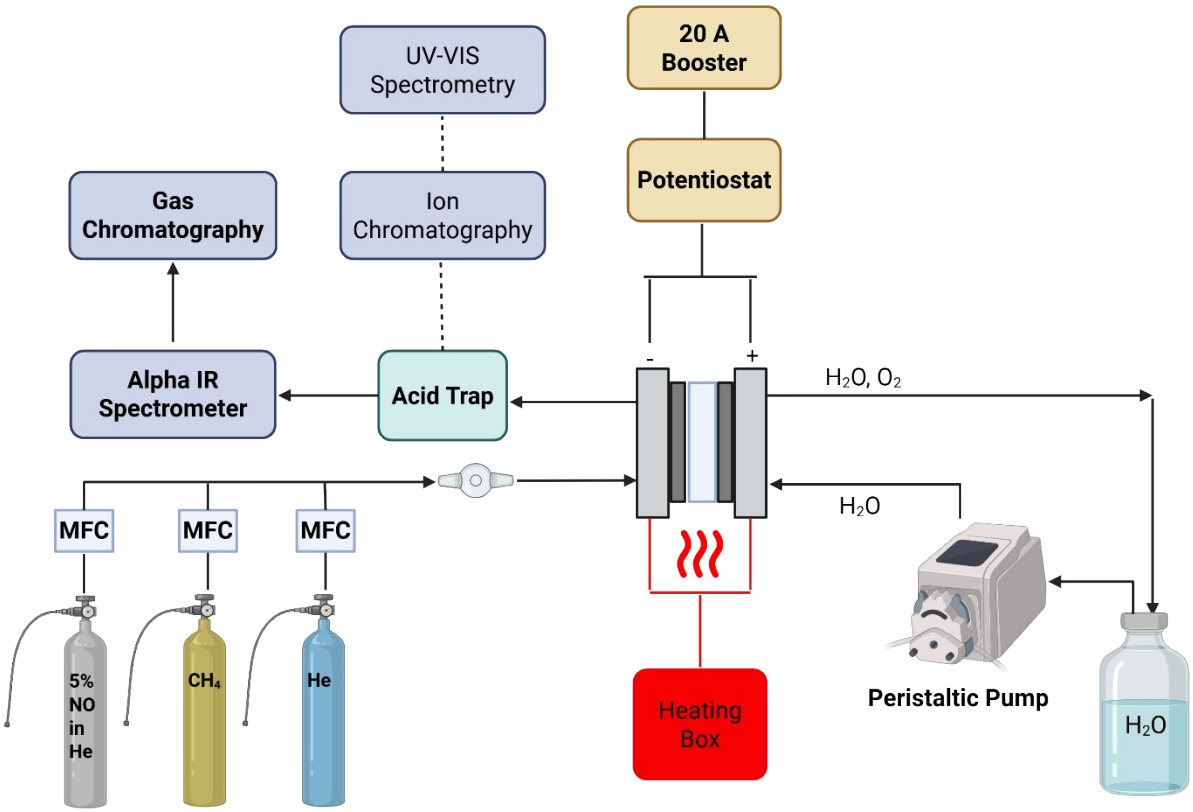

Figure S19. Experimental setup of electrochemical NO reduction.

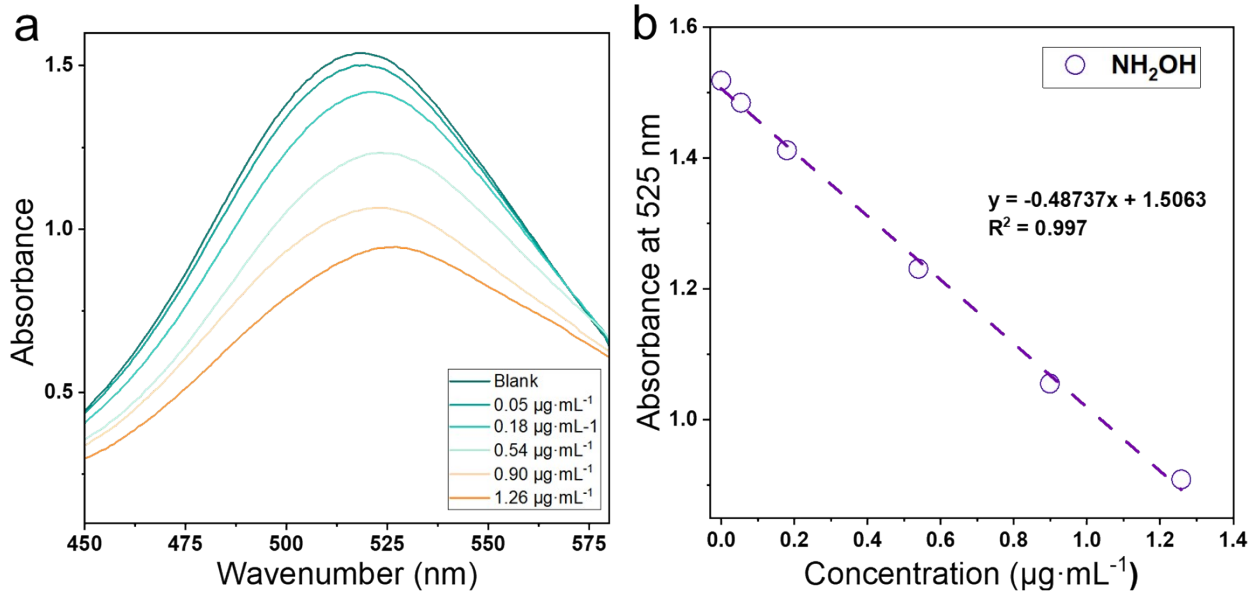

Figure S20. Neutral red method for hydroxylamine quantification. (a) UV-Vis absorption spectra of various hydroxylamine concentrations. (b) calibration curve for hydroxylamine quantification.

Catalyst	Electrolyzer	NO concentration	Liquid electrolyte	Potential	NH_3 FE (%)	NH_3 production rate μmol cm^{-2} h^{-1}
Co/Co_3O_4[1]	H cell	10% NO	0.1 M PBS	-0.6 V vs. RHE	94.7	340.4
S-Cu@Co/C[2]	H cell	10% NO	0.1 M PBS	-0.6 V vs. RHE	92.4	655.3
Mo_2C[3]	H cell	99.99% NO	0.5 M Na_2SO_4	-0.4 V vs. RHE	86.3	122.7
CuNi@BCN[4]	Flow cell	10% NO	PBS	−0.5 V vs. RHE	95.1	573.7
Co_1/MoS_2[5]	H cell	99.99% NO	0.5 M Na_2SO_4	-0.5 V vs. RHE	87.7	217.6
Cu nanowire array[6]	H-type high-pressure electrolyze	99.9% NO	1 M KOH	-0.4 V vs. RHE	96.1	10500
Porous Ni (DHBT Ni on GDL)[7]	AEM	1% NO	No	100 mA/cm^2	92	556
Cu_6Sn_5[8]	Flow cell	70% NO	0.5 M KOH	>1.400 mA/cm^2	96	10000
$CoMn_2O_4/C$[9]	H-cell	99.9% NO	0.1 M Na_2SO_4	−0.7 V vs. RHE	89.3	497.6
40 wt% Ru/C[10]	PEM	5.2% NO	No	1.9 V	93	510
50 wt.% MoS_2/C	PEM	5% NO	No	2.3 V	64.5	558

Table S4. Comparison of NH_3 production rate vs. potential from reported studies.

Reference

1. X. Fan, L. Han, Y. Bi, J. Song, X. Li, H. Duan and D. Zhang, *Applied Catalysis B: Environment and Energy*, 2025, **375**, 125416.
2. Z. Wang, H. Duan, W. Qu, D. Han, X. Li, L. Zhu, X. Jiang, D. Cheng, Y. Shen, M. Xie, E. Cortes and D. Zhang, *Angewandte Chemie International Edition*, 2025, **64**, e202511398.
3. K. Chen, P. Shen, N. Zhang, D. Ma and K. Chu, *Inorganic Chemistry*, 2023, **62**, 653-658.
4. Z. Wang, H. Duan, W. Qu, H. Zhang, L. Han, Z. Teng, G. Chen, D. Cheng, X. Wang, Y. A. Wu, M. Xie and D. Zhang, *Advanced Functional Materials*, 2025, **35**, 2507533.
5. X. Li, K. Chen, X. Lu, D. Ma and K. Chu, *Chemical Engineering Journal*, 2023, **454**, 140333.
6. W. Yang, H. Liu, X. Chang, Y. Zhang, Y. Cai, Y. Li, Y. Cui, B. Xu, L. Yu, X. Cui and D. Deng, *Nature Communications*, 2025, **16**, 1257.
7. A. Singh-Morgan, K. Trösch, A. Weinfurter, M. Inniger, Y.-Z. Xu and V. Mougel, *Chem*, 2025, **11**, 102460.
8. J. Shao, H. Jing, P. Wei, X. Fu, L. Pang, Y. Song, K. Ye, M. Li, L. Jiang, J. Ma, R. Li, R. Si, Z. Peng, G. Wang and J. Xiao, *Nature Energy*, 2023, **8**, 1273-1283.
9. Z. Niu, S. Fan and X. Li, *Journal of Materials Chemistry A*, 2024, **12**, 19988-19994.
10. S. Bunea, M. Coppens and A. Urakawa, *ACS Catalysis*, 2023, **13**, 11345-11351.